Multifrequency Wireless Channel Measurements and Characterization in Large Indoor Office Environments

Li Zhang, *Student Member, IEEE*, Cheng-Xiang Wang, *Fellow, IEEE*, Zihao Zhou, Xinyue Chen, *Student Member, IEEE*, Jie Huang, *Member, IEEE*, Chun Pan, El-Hadi M. Aggoune, *Life Senior Member, IEEE*, and Yang Miao, *Member, IEEE*

***Abstract*— This article performs extensive channel measurements and characteristics analysis to investigate large-scale fading (LSF) and small-scale fading (SSF) of wireless local area network (WLAN) channels in large indoor office environments. Multifrequency single-input–single-output (SISO) channel measurements are conducted at 3, 5.5, and 6.5 GHz under the same conditions to explore the frequency dependence of LSF, delay spread (DS), and K-factor (KF). Then, SISO channel measurements with different half-power beamwidths (HPBWs) of antennas are performed at 5.5 GHz in access point (AP) to user equipment (UE) and AP-to-AP scenarios. The effects of antenna HPBW on LSF, DS, and KF are investigated, thereby inspiring the AP deployment in high-density (HD) scenarios. Finally, 32 × 64 multiple-input–multiple-output (MIMO) channel measurements at 5.5 GHz are conducted to study the SSF of the time nonstationarity and multilink correlation. The time nonstationarity, including the parameters' drifting and cluster evolution caused by the movement of the UE, is verified by the measurement results. Multilink correlations are illustrated from the perspectives of the angular power spectral density (APSD) and correlation matrix collinearity (CMC). The results show that the distance between users and separation angle can affect the multilink correlation.**

***Index Terms*— Antenna beamwidth, large indoor office environments, multifrequency wireless channel measurements, multilink correlations, time nonstationarity.**

Manuscript received 27 July 2022; revised 20 January 2023; accepted 15 February 2023. Date of publication 24 March 2023; date of current version 2 June 2023. This work was supported in part by the National Key Research and Development Program of China under Grant 2018YFB1801101; in part by the National Natural Science Foundation of China (NSFC) under Grant 61960206006 and Grant 62271147; in part by the Key Technologies Research and Development Program of Jiangsu (Prospective and Key Technologies for Industry) under Grant BE2022067 and Grant BE2022067-1; in part by the EU Research and Innovation Staff Exchange (RISE) project under Horizon2020 Testing and Evaluating Sophisticated information and communication Technologies for enaBling scalablE smart griD Deployment (TESTBED2) Project under Grant 872172; in part by the High Level Innovation and Entrepreneurial Doctor Introduction Program in Jiangsu under Grant JSSCBS20210082; and in part by the University of Tabuk, Saudi Arabia, under Grant 1444-154. *(Corresponding authors: Cheng-Xiang Wang; Jie Huang.)*

Li Zhang, Cheng-Xiang Wang, Zihao Zhou, Xinyue Chen, and Jie Huang are with the National Mobile Communications Research Laboratory, School of Information Science and Engineering, Southeast University, Nanjing 210096, China, and also with the Purple Mountain Laboratories, Nanjing 211111, China (e-mail: li-zhang@seu.edu.cn; chxwang@seu.edu.cn; zhouzihao@seu.edu.cn; chenxinyue_2019@seu.edu.cn; j_huang@seu.edu.cn).

Chun Pan is with Huawei Technologies Company Ltd., Nanjing 210012, China (e-mail: panchun@huawei.com).

El-Hadi M. Aggoune is with the Sensor Networks and Cellular Systems Research Center, University of Tabuk, Tabuk 71491, Saudi Arabia (e-mail: hadi.aggoune@gmail.com).

Yang Miao is with the Faculty of Electrical Engineering, Mathematics and Computer Science, University of Twente, 7522 NB Enschede, The Netherlands (e-mail: y.miao@utwente.nl).

Color versions of one or more figures in this article are available at https://doi.org/10.1109/TAP.2023.3259736.

Digital Object Identifier 10.1109/TAP.2023.3259736

I. Introduction

WIRELESS local area network (WLAN) and cellular mobile communication are two major wireless communication technologies that complement each other in realizing the intelligent Internet of Things (IoT) [1], [2], [3], [4]. Multifrequency cooperation and multiuser multiple-input–multiple-output (MU MIMO) technologies are introduced by the next-generation IEEE 802.11be standard to improve the spectrum efficiency and network throughput [5], [6], [7]. Currently, wireless fidelity (Wi-Fi) networks are working at 2.4 GHz and 5 GHz. However, the limited spectrum resources cannot meet the requirements of rapidly growing wireless devices. Fortunately, the 6-GHz band will be open for Wi-Fi, and the devices are enabled to simultaneously work at 2.4, 5, and 6 GHz [8]. The three frequency bands can cooperate to fulfill the high speed, large capacity, and low latency demands. In addition, the MU MIMO technology uses spatial diversity of channels to provide more spatial streams for multiple users with the same bandwidth, which greatly improves the throughput. The time nonstationarity and multilink correlation are two important channel characteristics for the MU MIMO technology, and they will affect system performance evaluation. Besides the two physical layer technologies, the antenna beamwidth also influences the network capacity. In high-density (HD) scenarios, there is a relatively high concentration of wireless terminals [10], resulting in worse communication quality. Using narrow beamwidth antennas, more high-gain access points (APs) can be deployed to serve more user equipment (UE) with less interference between APs. In conclusion, exploring the multifrequency and MU MIMO channel properties and investigating the impacts of antenna beamwidth are important for efficient communication systems' design, deployment, and optimization [9].

The existing multifrequency channel measurements are mainly concentrated on comparisons between millimeter-wave (mmWave) bands and sub-6-GHz bands. Channel measurements were performed at 6.75, 30, and 60 GHz in a street

canyon scenario [11], a large indoor corridor scenario [12], and a corner environment [13]. Directional scanning channel measurements from 2.4 to 61 GHz were carried out in a semi-open office and a closed office [14]. Multifrequency characteristics for classroom and hall scenarios at 2–4-, 9–11-, and 27–29-GHz bands were analyzed in [15]. In addition, some multifrequency measurements investigated the frequency dependence of statistical properties for ultrawideband (UWB) channels. In [16], channel measurements were conducted at 5–6.6 GHz in six different office environments. The frequency dependence of polarized UWB channel parameters at 2–5 GHz was explored in [17]. In [18], the frequency dependence of fading statistics was investigated for UWB systems at 3.1–10.6 GHz. Zhou et al. [19] performed channel measurements at 2.4, 5, and 6 GHz in the corridor scenario. However, few works studied multifrequency channel measurements at the three Wi-Fi frequency bands in a large office environment.

High-gain directional antennas instead of low-gain omnidirectional antennas are preferred at mmWave bands to compensate for the severe path loss (PL). Therefore, most of the existing channel measurements [20], [21], [22], [23], [24] focused on the effects of antenna beamwidth at mmWave bands. However, there are few studies of beamwidth effects at sub-6-GHz bands. Investigating the antenna beamwidth at sub-6 GHz is useful to determine and deploy AP antennas in HD scenarios.

Time nonstationarity is an important channel property and it is reflected by time-variant parameters and the cluster birth–death process [25], [26], [27]. The time variance of a wireless channel is caused by the relative movement between the transceiver and the scatterers. Consequently, the small-scale parameters (SSPs), i.e., delay and angle, are drifting smoothly. The multilink analysis based on channel measurements includes the correlation of large-scale parameters (LSPs) [28], [29], [30], [31], [32], [33] and correlation matrix [34], [35]. The early studies [28], [29], [30], [31] mainly focused on the multilink correlation of shadowing fading (SF) and delay spread (DS). Except for the SF and DS, correlation characteristics of K-factor (KF) were also investigated in high-speed railway scenarios [32], [33]. Oestges and Czink [34] measured the channel matrix of 16 links and analyzed the correlation matrix distance at the transmitting side. In [35] and [36], the correlation matrix collinearity (CMC) of multilink channels was calculated. The SSPs are important parts of channel models, and the correlation of SSPs also has significant impacts on the system performance. However, the channel measurements mentioned above did not evaluate the similarity of SSPs of different links.

In the existing works, there have been some relevant multifrequency channel measurements for UWB channels and comparisons between sub-6-GHz bands and mmWave bands, and multilink correlation analysis of LSPs and correlation matrix. However, channel measurements and analysis comparing the fading characteristics at three Wi-Fi bands under the same conditions, exploring the effects of antenna beamwidth in HD scenarios, and evaluating the multilink correlation of SSPs are still missing. Understanding channel characteristics and accurate channel modeling are the basis of wireless system design. Hence, investigating the corresponding WLAN channel properties is of vital importance to establish accurate large-scale fading (LSF) and small-scale fading (SSF) channel models, and to further optimize WLAN system performance. To fill the above gaps, extensive channel measurements in a large indoor office environment are conducted. The main contributions and novelties of this article are summarized as follows.

1) Multifrequency single-input–single-output (SISO) channel measurements are conducted at 3, 5.5, and 6.5 GHz under the same measurement conditions. Based on the channel measurements, the channel characteristics of LSF, DS, and KF are investigated at these three Wi-Fi bands.
2) SISO channel measurements with different half-power beamwidths (HPBWs) of antennas are performed at 5.5 GHz. Furthermore, the effects of antenna HPBW on LSF, DS, and KF are studied and compared in the AP–UE and AP–AP scenarios.
3) The 32 $\times$ 64 multiple-input–multiple-output (MIMO) channel measurements are conducted at 5.5 GHz to explore the SSF of the time nonstationarity and multilink correlation. The time nonstationarity is demonstrated by the delay power spectral density (DPSD) and angle drifting. The multilink correlations are investigated by the angular power spectral density (APSD) and CMC.

The rest of this article is organized as follows. Section II describes the channel measurement equipment, environment, and configuration. In Section III, a brief description of measurement data processing procedure is introduced. Channel measurement results and analysis are presented in Section IV. Finally, conclusions are drawn in Section V.

II. Channel Measurements

A. Channel Sounding System

The Keysight time-domain channel sounder is used to conduct channel measurements. It mainly includes a transmitter (Tx) side and a receiver (Rx) side, as shown in Fig. 1. The Tx side is composed of an arbitrary waveform generator M8190A, a power amplifier, and a radio frequency (RF) switch supporting 32 channels' measurements in serial. The Rx side consists of a wideband digitizer M9703B, an analog signal generator N5173B, eight down converters, eight intermediate frequency (IF) amplifiers, and eight RF switches to support 64 channels' measurements. A pair of high-precision rubidium clocks and GPS antennas are used to provide 1 pulse/s (1 PPS) and 10-MHz reference clock for the synchronization of the Tx and Rx.

The pseudonoise (PN) sequence is used as the sounding signal and downloaded to M8190A. Then, the output RF signal is amplified by the power amplifier and transmitted through antenna arrays for MIMO channel measurements. Each antenna element is switched by high-speed RF switches with a switch time of 1 μs. The IF signal is obtained by the mixture of the received RF signal and the local oscillator signal. To improve the signal-to-noise ratio (SNR), the IF signal is amplified by the IF amplifier first, and then sampled

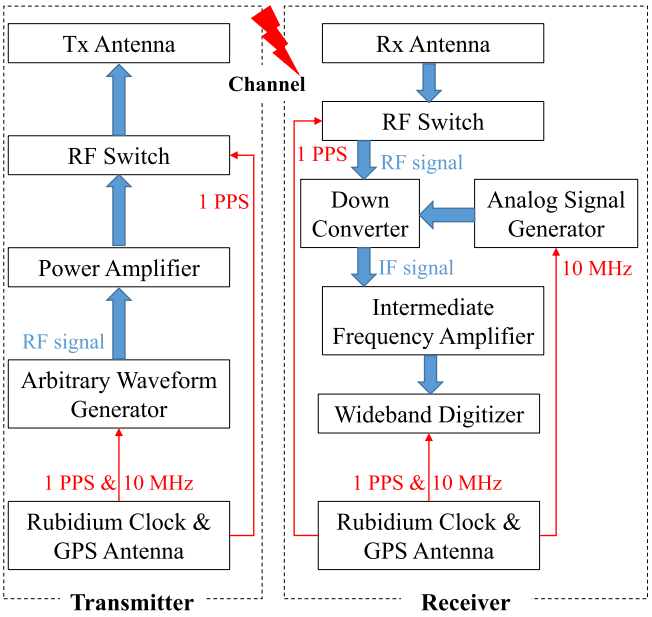

Fig. 1. Diagram of the channel measurement system.

Fig. 2. Photograph of the large indoor office environment.

by M9703B with a sampling rate of 1.6 GSa/s. Finally, the downconverting operation is completed by the Keysight VSA 89 600 software, and the baseband IQ data are stored on the server. For SISO channel measurements, the RF switch is not necessary, and other steps are similar to MIMO channel measurements.

B. Measurement Environment and Setup

The measurement campaign was carried out in a typical large indoor office environment with a size of 50 × 17 × 3.3 m^3, and the environment is illustrated in Fig. 2. The office is equipped with nearly 100 working seats. Each seat is at 0.75-m height at the desktop level and with an additional vertical clapboard having about 0.45-m height. There are one or two monitors and other small objects on desks. The office is surrounded by glass windows, metal walls, and metal ceiling. Besides, there are 12 metal pillars. This office is similar to the indoor hotspot scenario defined in [37], and there exist large number of connected devices.

Three channel measurement cases with different configurations are conducted in the office environment in line-of-sight (LOS) and non-LOS (NLOS) scenarios. Multifrequency SISO channel measurements in Case 1 are used to investigate the channel characteristics of LSF, DS, and KF at two existing Wi-Fi bands and the newly introduced 6-GHz band. SISO channel measurements in Case 2 are performed at 5.5 GHz to study the effects of antenna HPBW on LSF, DS, and KF in the AP–UE and AP–AP scenarios. In Case 3, 32 × 64 MIMO channel measurements are conducted at 5.5 GHz. Then, the time nonstationarity and multilink correlation are analyzed.

1) Case 1: The bandwidths of all the cases are 320 MHz, and the center frequencies of Case 1 are 3, 5.5, and 6.5 GHz. The results in [19] show that there is strong interference at 2.4 GHz, and therefore 3 GHz is chosen instead in this article. To ensure the same measurement conditions, 2–8-GHz omnidirectional antennas (abbreviated as omni in the following figures and tables) are used at Tx and Rx sides. The channel measurements at three frequency bands are conducted at different time instants. During channel measurements, there are no walking person and moving objects. Therefore, the measurement environment can be considered as quasi-static, and channel measurements at different time instants do not affect the channel characteristics. The Tx antenna is mounted upside down from the ceiling with a height of 3.3 m. The heights of the Rx antenna are 1.5 m in the aisle (referred to as RxH) and 0.75 m in the working seat (referred to as RxL). Fig. 3 gives a detailed description of the office layout and measurement positions. The metal pillars are numbered by "P1-1" to "P6-1" and "P1-2" to "P6-2."

2) Case 2: In the AP–UE scenario (Case 2-1), the height of the Tx antenna is 3.3 m and the height of the Rx antenna is 1.5 or 0.75 m. Three different antennas are used as the Tx antenna, i.e., directional antenna, elevation HPBW (EHPBW) < 90° omnidirectional antenna, and EHPBW > 120° omnidirectional antenna. The measurement positions are the same as Case 1. In the AP–AP scenario (Case 2-2), antennas of both the sides are the same type and they are mounted upside down from the ceiling. The antennas are EHPBW = 90° omnidirectional antenna, EHPBW = 120° omnidirectional antenna, and 2–8 GHz omnidirectional antenna whose EHPBW is larger than 120°. There are three Tx positions, and 45 Rx positions for each Tx position.

3) Case 3: The Tx antenna is 32-element uniform planar array (UPA) with four dual-polarized antenna elements uniformly placed on each row and each column. The Rx antenna is 64-element uniform circular array (UCA) with four rings and eight dual-polarized antenna elements uniformly placed on each ring. The measurement positions and local coordinate systems (LCSs) of the Tx and Rx antennas are illustrated in Fig. 4. Totally, 88 positions (referred to as RxH) are measured, and there are two long routes where Rx positions are spaced by 0.5 m. Among all the measurement positions, RxH70–75 and RxH87 are obstructed by the

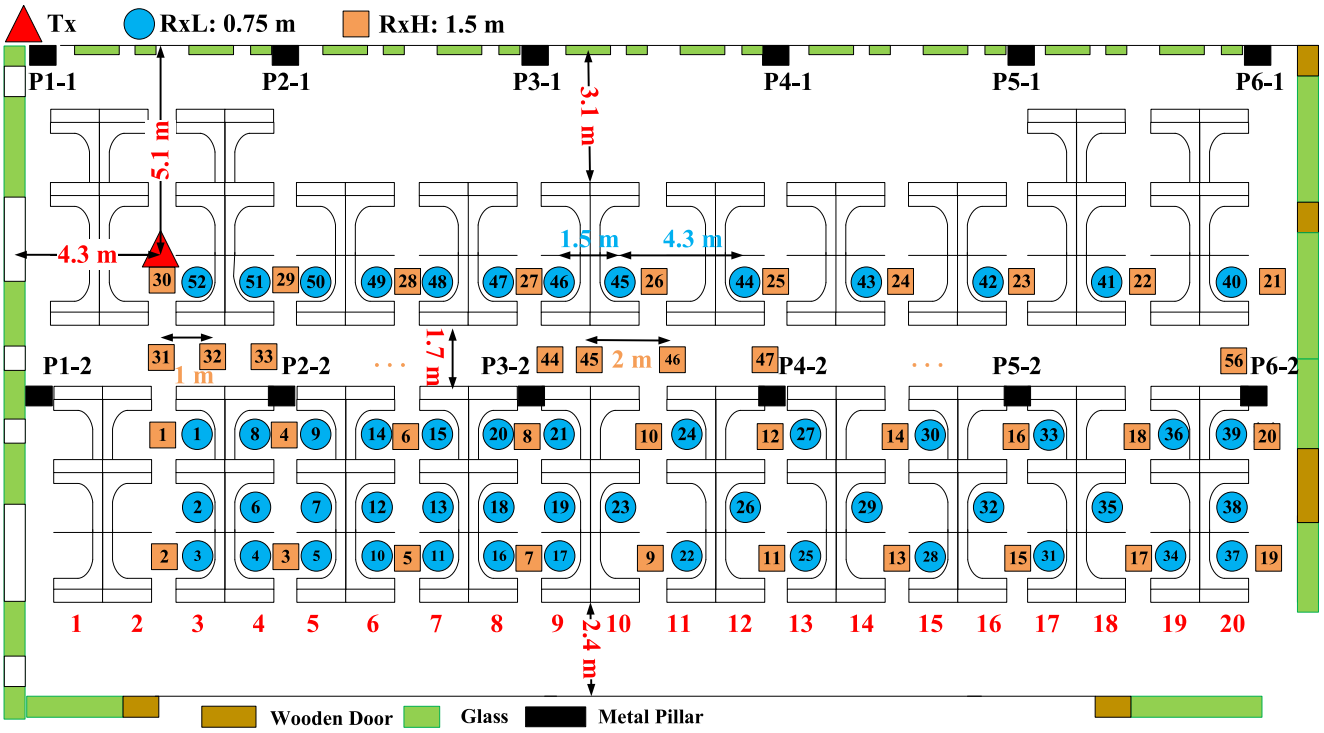

Fig. 3. Office layout and measurement positions of Case 1 and Case 2-1.

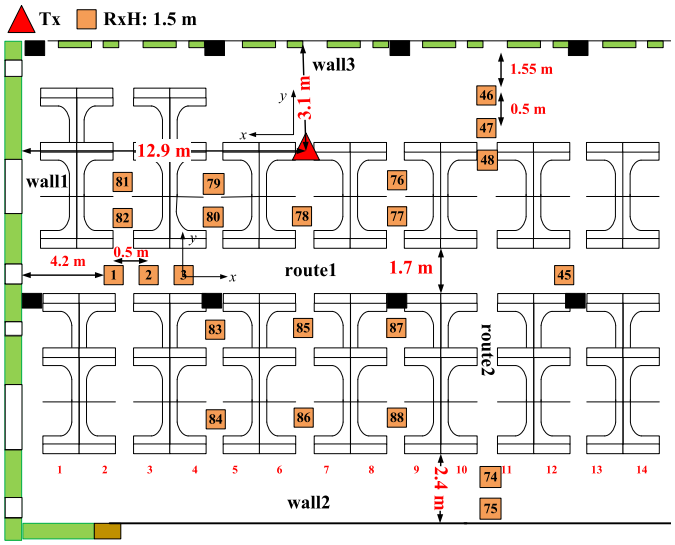

Fig. 4. Measurement positions of Case 3.

metal pillar "P3-2." Therefore, these positions are NLOS positions and the others are LOS positions. The measurement configuration and parameters for all the cases are summarized in Table I.

4) Calibration: Calibration operation is needed to remove the measurement system response. For SISO channel measurements, back-to-back calibration is completed by connecting the output of the power amplifier and the input of the downconverter with a 60-dB attenuator. To obtain the calibration data of 32 × 64 MIMO channels, the first step is to measure the frequency responses of RF switches at Tx and Rx sides and a power splitter by the vector network analyzer. Then, the transmitted signal from one channel of the RF switch at the Tx side is connected to eight parallel channels at the Rx side by the power splitter. To ensure that the received power is not saturated, a 40-dB attenuator is used. Finally, the calibration data of other 56 channels can be reconstructed by their frequency responses and the eight channels' back-to-back calibration data.

TABLE I
CONFIGURATIONS AND PARAMETERS OF CHANNEL MEASUREMENTS

Cases	Frequency (GHz)	Antenna Type	Antenna Height (m)	Measurement Positions
1	3, 5.5, 6.5	Tx, Rx: 2-8 GHz omni	Tx: 3.3 RxH: 1.5 RxL: 0.75	Tx: 1 RxH: 56 RxL: 52
2-1	5.5	Tx: directional, EHPBW<90° omni, EHPBW>120° omni Rx: 2-8 GHz omni	Tx: 3.3 RxH: 1.5 RxL: 0.75	Tx: 1 RxH: 56 RxL: 52
2-2	5.5	Tx, Rx: EHPBW=90° omni, EHPBW=120° omni, 2-8 GHz omni	Tx: 3.3 Rx: 3.3	Tx: 3 Rx: 45
3	5.5	Tx: 32 elements UPA Rx: 64 elements UCA	Tx: 2.9 Rx: 1.5	Tx: 1 Rx: 88

III. MEASUREMENT DATA PROCESSING

A. Calculation of Channel Impulse Response (CIR)

Let $\boldsymbol{s}(t)$ denote the transmitted signal. The system response of the channel sounder can be obtained in the back-to-back calibration process and it is represented by $\boldsymbol{h}_{\text{sys}}(t)$. Hence, the calibrated signal can be expressed by $\boldsymbol{y}_{\text{sys}}(t) = \boldsymbol{s}(t) * \boldsymbol{h}_{\text{sys}}(t)$, where $*$ represents the convolution operation. The wireless

CIR is denoted by $\boldsymbol{h}(t)$ and the wireless received signal can be calculated as $\boldsymbol{y}(t) = \boldsymbol{s}(t) * \boldsymbol{h}_{\text{sys}}(t) * \boldsymbol{h}(t)$. Therefore, the wireless CIR is obtained by the operation of inverse fast Fourier transform (IFFT) [38] as

$$\boldsymbol{h}(t) = \text{IFFT}\left\{\frac{\mathbf{Y}(f)}{\mathbf{Y}_{\text{sys}}(f)}\right\} = \text{IFFT}\left\{\frac{\text{FFT}(\boldsymbol{y}(t))}{\text{FFT}\big(\boldsymbol{y}_{\text{sys}}(t)\big)}\right\} \quad (1)$$

where $\mathbf{Y}_{\text{sys}}(f)$ and $\mathbf{Y}(f)$ are the frequency responses of $\boldsymbol{y}_{\text{sys}}(t)$ and $\boldsymbol{y}(t)$, respectively.

B. Outlier Snapshots Elimination

For each measurement data, it is observed that a few snapshots have significant difference compared with the rest. To improve the accuracy of the data, outlier snapshots are deleted to ensure that all the remaining snapshots are perfectly correlated. The calculation of snapshot correlation can be referred to [39]. Let $\mathbf{H}_{s_1}(f)$ and $\mathbf{H}_{s_2}(f)$ be the channel transfer functions of s_1th and s_2th snapshots between a given Tx–Rx antenna pair, respectively. The symmetric correlation matrix is calculated as $\mathbf{Q} = [|\mathbf{H}_{s_1}(f)^H \mathbf{H}_{s_2}(f)|]_{S\times S}$, where $(\cdot)^H$ means the Hermitian operation and S is the number of snapshots. The $1 \times S$ vector of column summation of matrix $\mathbf{Q}$ is represented by $\boldsymbol{g}$. We keep the snapshots when the corresponding entries of the vector $\boldsymbol{g}$ are only 1% different from the median of $\boldsymbol{g}$. The effective snapshots are averaged to calculate the DPSD.

C. Parameters' Estimation

The peak search algorithm [40] is used to extract multipath components (MPCs) from the DPSD. MPCs and noise are commonly distinguished by applying a threshold, which lies 6 dB above the noise floor [41]. If the SNR is high enough, the threshold can be determined by the larger value of 10 dB above the noise floor and 20 dB below the maximum power [40]. The SNR values of all the measurement positions are above 35 dB. The received power P_{r} is estimated by summing the power of all MPCs' path gains

$$P_{\text{r}} = \sum_{l=1}^{L} P_l \quad (2)$$

where P_l represents the power of the lth path, and L represents the total number of MPCs.

The estimated dual-polarized MIMO propagation channel can be characterized by

$$\hat{\boldsymbol{h}}(t;\boldsymbol{\theta}_l) = \sum_{l=1}^{L} \exp(j2\pi\nu_l t) \sum_{p_1=1}^{2}\sum_{p_2=1}^{2} \alpha_{l,p_1,p_2}\boldsymbol{c}_{2,p_2}\big(\boldsymbol{\Omega}_{2,l}\big) \times \boldsymbol{c}_{1,p_1}\big(\boldsymbol{\Omega}_{1,l}\big)^T \delta(\tau-\tau_l). \quad (3)$$

In (3), the parameters' set of the lth MPC is denoted by $\boldsymbol{\theta}_l = [\boldsymbol{\Omega}_{1,l}, \boldsymbol{\Omega}_{2,l}, \tau_l, \nu_l, \alpha_{l,p_1,p_2}]$, which includes propagation delay τ_l, the direction of departure $\boldsymbol{\Omega}_{1,l}$, the direction of arrival $\boldsymbol{\Omega}_{2,l}$, four complex amplitudes α_{l,p_1,p_2}, $p_1/p_2 = \{1,2\}$, and Doppler frequency ν_l. The directions are described as unit vectors in spherical coordinates, corresponding to $\boldsymbol{\Omega}_{1,l} = [\sin(\theta_{l,\text{EoD}})\sin(\phi_{l,\text{AoD}}),\ \sin(\theta_{l,\text{EoD}})\cos(\phi_{l,\text{AoD}}),\ \cos(\theta_{l,\text{EoD}})]^T$ and $\boldsymbol{\Omega}_{2,l} = [\sin(\theta_{l,\text{EoA}})\sin(\phi_{l,\text{AoA}}), \sin(\theta_{l,\text{EoA}})\cos(\phi_{l,\text{AoA}}), \cos(\theta_{l,\text{EoA}})]^T$. The angles $\phi_{l,\text{AoA/AoD}}$ and $\theta_{l,\text{AoA/AoD}}$ are the azimuth angle of arrival or departure (AAoA/AAoD) and elevation angle of arrival or departure (EAoA/EAoD), respectively. Besides, $\boldsymbol{c}_1(\boldsymbol{\Omega}_1)$ and $\boldsymbol{c}_2(\boldsymbol{\Omega}_2)$ are the antenna pattern of two kinds of polarization in the direction $\boldsymbol{\Omega}_1$ and $\boldsymbol{\Omega}_2$. The transpose operation is denoted by $(\cdot)^T$. The detailed parameters' estimation process of dual-polarized space-alternating generalized expectation–maximization (SAGE) algorithm can be referred to [42].

TABLE II
PARAMETERS OF CI AND FI MODELS IN LOS AND NLOS SCENARIOS

Cases	Conditions	Para-meters	LOS scenario		NLOS scenario	
			CI model	FI model	CI model	FI model
1	3 GHz	n	1.6	1.36	2.11	2.15
		σ	1.96	1.81	3.19	3.19
		β	41.94	44.77	41.94	41.38
	5.5 GHz	n	2.26	2.09	2.61	2.57
		σ	1.85	1.76	3.13	3.13
		β	47.21	49.31	47.21	47.71
	6.5 GHz	n	2.06	1.98	2.41	2.45
		σ	2.31	2.29	2.95	2.95
		β	48.66	49.66	48.66	48.19
2-1	EHPBW>120° omni	n	2.15	1.97	2.52	2.66
		σ	2.35	2.27	2.65	2.63
		β	47.21	49.52	47.21	45.26
	EHPBW<90° omni	n	2.55	2.86	2.95	3.13
		σ	2.37	2.16	2.7	2.68
		β	47.21	43.66	47.21	44.87
	directional	n	1.9	1.71	2.36	2.96
		σ	2.49	2.41	3.6	3.36
		β	47.21	49.52	47.21	39.16
2-2	EHPBW=120° omni	n	3.16	2.49	3.23	2.44
		σ	2.09	1.36	1.71	1.05
		β	47.21	56.2	47.21	58.07
	EHPBW=90° omni	n	3.36	2.59	3.4	2.62
		σ	1.94	1.21	1.85	1.26
		β	47.21	57.63	47.21	57.97
	2-8 GHz omni	n	2.7	2.49	2.74	2.69
		σ	1.43	1.36	1.26	1.26
		β	47.21	50.07	47.21	47.94

IV. RESULTS AND ANALYSIS

A. LSF, DS, and KF of SISO Measurements

1) LSF: The LSF models include the modeling of the PL and SF. The commonly used close-in (CI) PL model and floating intercept (FI) PL model [43], [44] are fit with the measurement data. The intercept of the CI PL model is a function of center frequency f_c and the PL exponent (PLE) n is a variable. The CI PL model is shown as

$$PL = 32.4 + 20\log_{10}(f_c) + 10n\log_{10}(d) + X_\sigma \quad (4)$$

where d is the distance between Tx and Rx, and X_σ is the SF, which can be modeled by a normal distribution variable with zero mean and standard variance of σ.

The intercept β in dB and the PLE of FI PL model are variables. The FI PL model is given by

$$PL = 10n\log_{10}(d) + \beta + X_\sigma. \quad (5)$$

The fitting parameters of the CI model and FI model are summarized in Table II. To keep consistency, we consider the value of $32.4 + 20\log_{10}(f_c)$ as the intercept of the CI model.

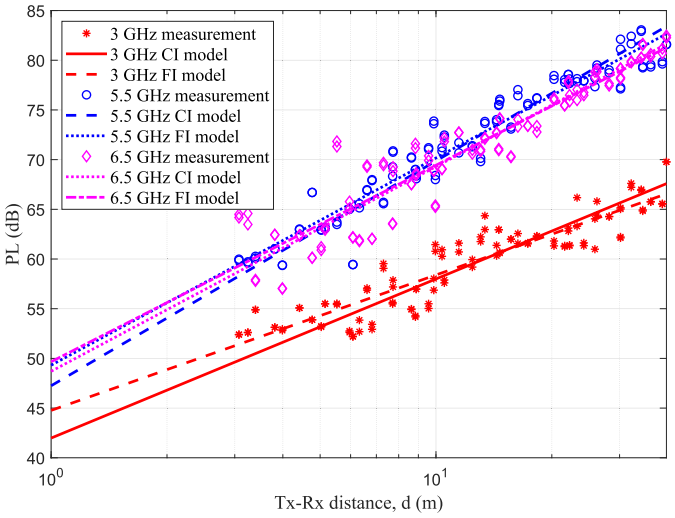

(a)

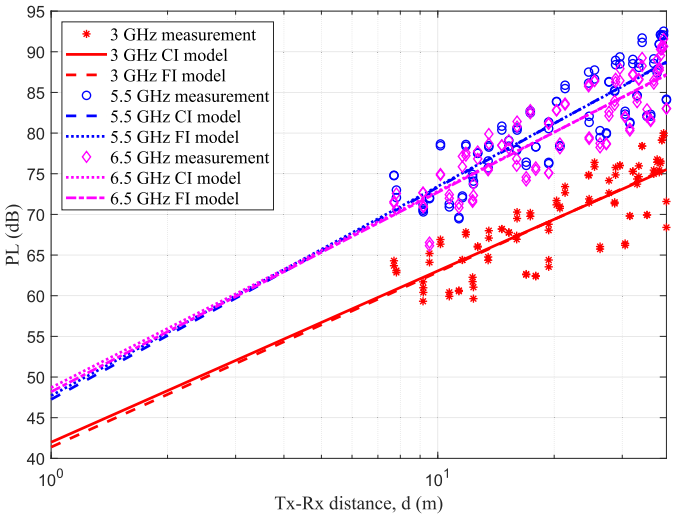

(b)

Fig. 5. Case 1: the PL of measurement results, the CI model, and FI model at 3, 5.5, and 6.5 GHz. (a) LOS scenarios. (b) NLOS scenarios.

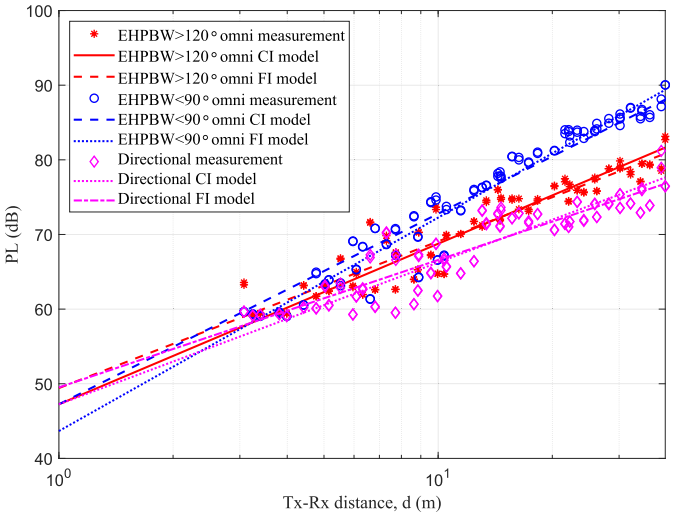

(a)

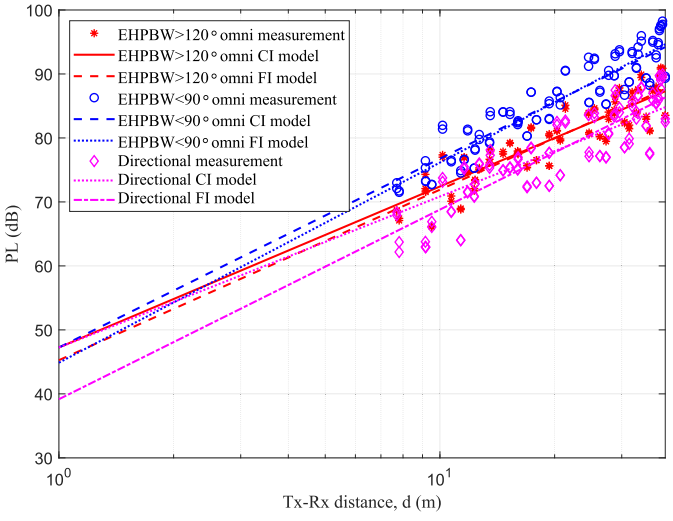

(b)

Fig. 6. Case 2-1: the PL of measurement results, the CI model, and FI model in the AP–UE scenario. (a) LOS scenarios. (b) NLOS scenarios.

Fig. 5 illustrates the PL of the measurement results, the CI model, and FI model at 3, 5.5, and 6.5 GHz. It is obvious that the PL at 3 GHz is much lower than that of 5.5 and 6.5 GHz in both the LOS and NLOS scenarios. However, there is no significant difference in the PL between 5.5 and 6.5 GHz. Observing from Table II, the PLE, SF, and intercept of the FI model and CI model have minor difference in the LOS scenarios and are almost the same in the NLOS scenarios. The PLE of 3 GHz is much smaller than those of the other two frequencies. The PLE and SF do not show a linear relationship with frequency. According to the results in [14] and [16], the frequency dependence of the PLE and SF strongly depends on the environment. Compared with the parameters in 3GPP TR 38.901 [45], we can find that the PLE of 3GPP TR 38.901 channel model at 3 GHz is higher, and the results at 5.5 and 6.5 GHz are lower than the measurement results in the LOS scenarios. In the NLOS scenarios, the PLE is larger than the measurement results of three frequency bands.

Fig. 6 shows comparison of the measurement and fitting results of a directional antenna and two omnidirectional antennas in the AP–UE scenario. The EHPBW $< 90°$ antenna shows the highest PL in both the LOS and NLOS scenarios. Owing to its narrower EHPBW, the LOS coverage area is limited. As a result, the PL difference among the three antennas is more apparent in the LOS scenarios with the increasing distance. The PLE of omnidirectional antennas has the tendency to increase with the increasing EHPBW, but the SF is independent of EHPBW. The PLE and intercept of EHPBW $> 120°$ antenna are similar to that of the 2–8-GHz omnidirection antenna in Case 1, which indicates the close performance of these two antennas. The directional antenna has the minimum PL and the maximum SF on account of its high gain and directionality. In conclusion, directional antennas are suitable for long-distance and narrow direction scenarios. According to the fitting results, the omnidirectional antennas with narrower EHPBW can also provide appropriate gains for users when AP and UE are close to each other.

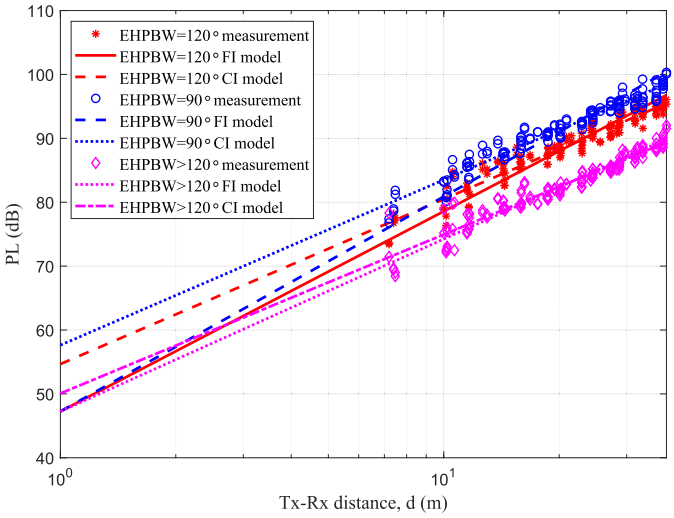

(a)

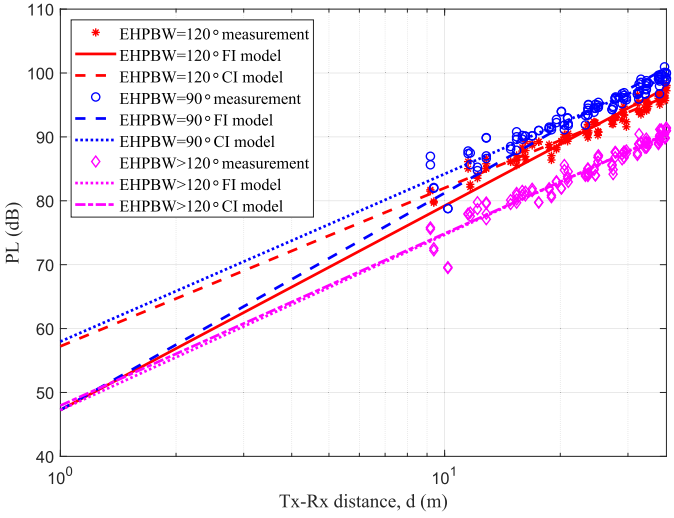

(b)

Fig. 7. Case 2-2: the PL of the measurement results, the CI model, and FI model in the AP–AP scenario. (a) LOS scenarios. (b) NLOS scenarios.

Fig. 7 shows comparison of the PL of three pairs of omnidirectional antennas in the AP–AP scenario. We can find that the PL increases with the decreasing EHPBW in both the LOS and NLOS scenarios, indicating that there may be a linear relationship between the PL and antenna beamwidth. The FI model parameters and CI model parameters of the EHPBW = 90° antenna and the EHPBW = 120° antenna are different from each other. For the CI model, the PLE has the negative relationship with EHPBW in the LOS and NLOS scenarios. For the FI model, the PLE and SF are almost the same among the three pairs of antennas. Furthermore, it can be concluded that omnidirectional antennas with narrower EHPBW have less power interference for adjacent APs.

2) DS: DS describes the channel time dispersion and it is calculated by delays and powers of all the MPCs

$$DS = \sqrt{\frac{\sum_{l=1}^{L} P_l \tau_l^2}{\sum_{l=1}^{L} P_l} - \left(\frac{\sum_{l=1}^{L} P_l \tau_l}{\sum_{l=1}^{L} P_l}\right)^2}. \tag{6}$$

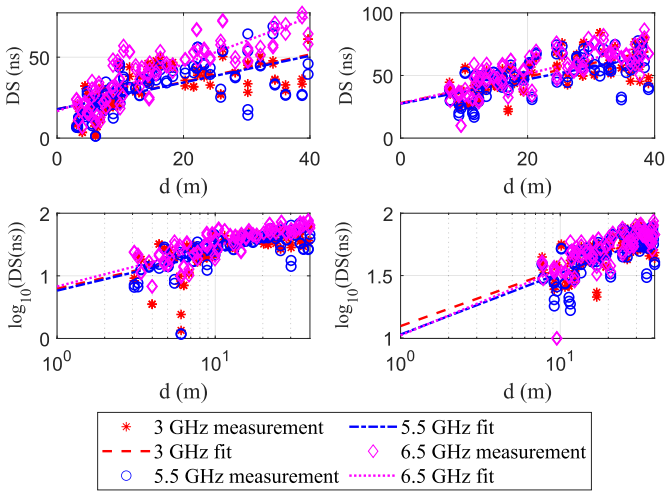

Fig. 8. Linear-distance and log-distance models of DS (the left two figures are the results in the LOS scenarios and the right two are the results in the NLOS scenarios).

The DS is found to increase with the increasing distance between Tx and Rx, and the relationship can be modeled by the linear-distance DS model [46] and the log-distance DS model [47]. The two models can be expressed by

$$DS(\text{ns}) = A \cdot d + B + DS_\sigma \tag{7}$$

and

$$\log_{10}(DS(\text{ns})) = A \cdot \log_{10}(d) + B + DS_\sigma \tag{8}$$

where A is the slope, B is the intercept, and DS_σ is the standard deviation. It can be deduced from Fig. 8 that DS increases with the increasing distance. As Rx is getting far away from Tx, the propagation environment is much more complicated, contributing to more MPCs and larger DS. The linear-distance model shows better fitting results in the NLOS scenarios than in the LOS scenarios. The log-distance model performs well in both the scenarios. In short, the log-distance model is easy to be adopted, because its fitting parameters have no frequency dependence. The fitting parameters of the log-distance model are $A = 0.6$, $B = 0.8$, and $DS_\sigma = 0.2$ and $A = 0.5$, $B = 1$, and $DS_\sigma = 0.1$ in the LOS and NLOS scenarios, respectively.

Log-normal distribution is used to fit the measurement results of DS, and the distribution parameters are given in Table III. The mean value is denoted as $\mu_{\lg(\text{DS(s)})}$, and the standard deviation is represented by $\sigma_{\lg(\text{DS(s)})}$, where $\lg(\cdot)$ is the abbreviation of $\log_{10}$.

Fig. 9 is the measurement and fitting results of DS at 3, 5.5, and 6.5 GHz. There is almost no frequency difference in DS and the DS is larger in the NLOS scenarios. There are 7.6-ns mean value difference in the LOS scenarios and 2.2-ns mean value difference in the NLOS scenarios among the three frequencies. In 3GPP TR 38.901 channel model [45], the mean value and standard deviation of DS are modeled as frequency-independent variables at sub-6 GHz. The measurement results are consistent with the 3GPP TR 38.901 channel model.

In the AP–UE scenario, the mean values of two omnidirectional antennas are the same in the LOS and NLOS

TABLE III
PARAMETERS OF DS IN LOS AND NLOS SCENARIOS

Cases	Conditions	LOS scenario		NLOS scenario	
		$\mu_{\lg(\mathrm{DS(s)})}$	$\sigma_{\lg(\mathrm{DS(s)})}$	$\mu_{\lg(\mathrm{DS(s)})}$	$\sigma_{\lg(\mathrm{DS(s)})}$
1	3 GHz	-7.58	0.29	-7.31	0.14
	5.5 GHz	-7.58	0.29	-7.33	0.16
	6.5 GHz	-7.47	0.25	-7.31	0.14
2-1	EHPBW>120° omni	-7.65	0.3	-7.35	0.19
	EHPBW<90° omni	-7.63	0.42	-7.35	0.2
	directional	-7.83	0.43	-7.44	0.2
2-2	EHPBW=120° omni	-7.29	0.14	-7.23	0.08
	EHPBW=90° omni	-7.28	0.13	-7.25	0.14
	2-8 GHz omni	-7.3	0.14	-7.26	0.12

scenarios. The standard deviations are different in the LOS scenarios but similar in the NLOS scenarios. It is shown that the EHPBW $< 90°$ antenna performs equally well in receiving reflected paths but worse in receiving LOS path compared with the EHPBW $> 120°$ antenna. The power of LOS path decreases when the Rx is out of the beam range in the LOS scenarios, resulting in larger standard deviation. The directional antenna exhibits the smallest DS because of its directionality. In the AP–AP scenario, the DS is independent of scenarios and antenna EHPBW. Since the Tx and Rx antennas are mounted upside down from the ceiling, most of the received paths are reflected paths, and the number of MPCs is more than that in the AP–UE scenario.

3) KF: The frequency-domain moment estimation method of wideband channel was proposed in [48]. It is suitable for KF estimation in static and wideband conditions. The estimated KF is calculated by

$$G_a = \frac{1}{M_f}\sum_{k=1}^{M_f}|\mathbf{H}(f)|^2 \tag{9}$$

$$G_v = \frac{1}{M_f - 1}\left(\sum_{k=1}^{M_f}|\mathbf{H}(f)|^4 - M_f G_a^2\right) \tag{10}$$

$$KF = \frac{\sqrt{G_a^2 - G_v}}{G_a - \sqrt{G_a^2 - G_v}} \tag{11}$$

where $\mathbf{H}(f) \in \mathbb{C}^{1\times M_f}$ is the channel transfer function of a given Tx–Rx antenna pair, $|\cdot|$ is the absolute value, and M_f is the number of frequency points. G_a and G_v are the second-order and fourth-order moments of $\mathbf{H}(f)$, respectively.

The normal distribution parameters of KF in dB are given in Table IV. The mean value and standard deviation are denoted as $\mu_{\lg(\mathrm{KF})}$ and $\sigma_{\lg(\mathrm{KF})}$, respectively. The KF decreases with the increasing frequency in the LOS scenarios and shows no frequency dependence in the NLOS scenarios. The mean value is smaller than that in [45], because the results rely on the measurement environment. Some Rx positions are far from the Tx with more MPCs, but they are in the LOS scenarios. In the AP–UE scenario, the KF of the directional antenna is the largest and that of the EHPBW $< 90°$ antenna is the smallest because of the increasing MPCs and decreasing LOS path power. Besides, there is no obvious antenna beamwidth dependence in the AP–AP scenario. The negative mean values in Table IV are due to the high power of reflected paths.

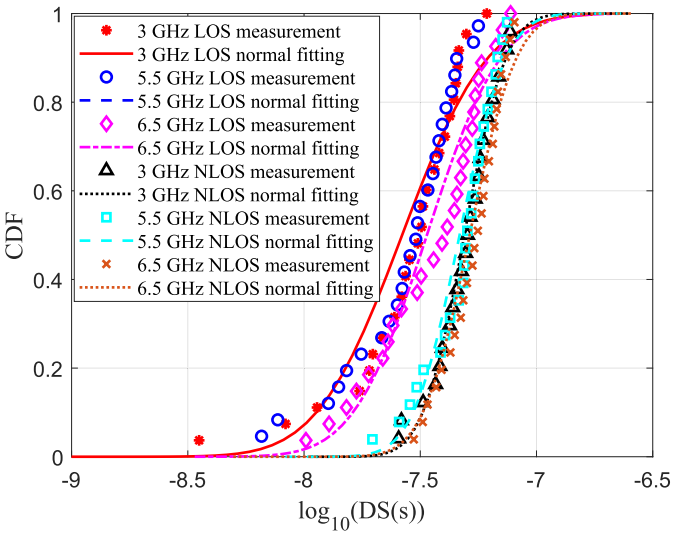

Fig. 9. Case 1: the DS of measurement and fitting results at 3, 5.5, and 6.5 GHz.

TABLE IV
PARAMETERS OF KF IN LOS AND NLOS SCENARIOS

Cases	Conditions	LOS scenario		NLOS scenario	
		$\mu_{\lg(\mathrm{KF})}$	$\sigma_{\lg(\mathrm{KF})}$	$\mu_{\lg(\mathrm{KF})}$	$\sigma_{\lg(\mathrm{KF})}$
1	3 GHz	2.12	5.4	-2.15	3.16
	5.5 GHz	0.57	4.77	-2.12	3.78
	6.5 GHz	0.08	4.21	-2.69	3.16
2-1	EHPBW>120° omni	2.65	5.51	-2.82	4.39
	EHPBW<90° omni	1.2	6.64	-2.76	3.95
	directional	4.24	6.28	-0.51	5.4
2-2	EHPBW=120° omni	-2.52	3.44	-4.11	3.35
	EHPBW=90° omni	-2.97	3.1	-3.74	4.19
	2-8 GHz omni	-3.07	2.97	-3.79	3.37

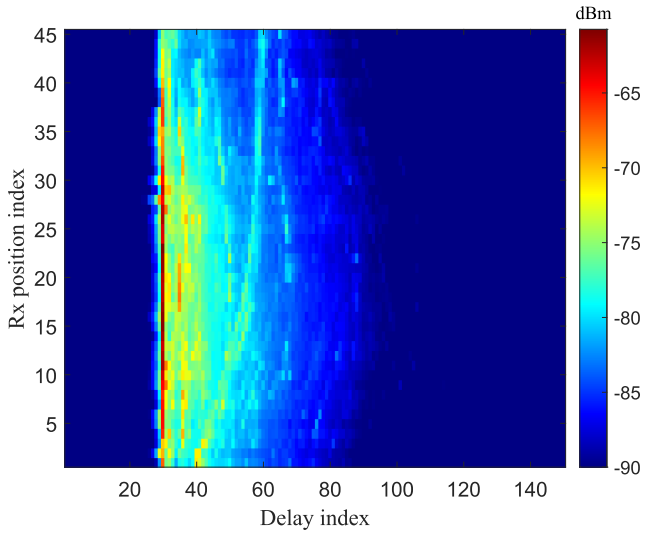

Fig. 10. Measured DPSD along route 1.

B. SSF of MIMO Measurements at 5.5 GHz

1) Time Nonstationarity: Here, time nonstationarity, including parameters drifting and cluster evolution, is caused by the movement of the Rx. Fig. 10 is an illustration of the measured DPSD along route 1 where there are 45 Rx positions. These

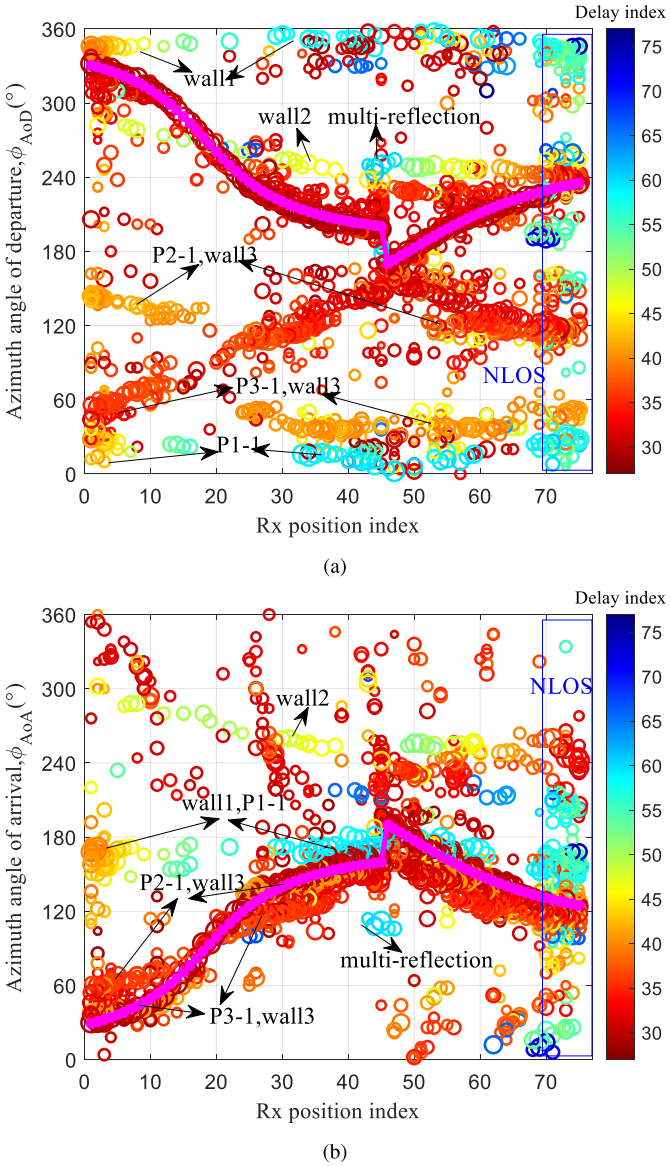

Fig. 11. Angle drifting and cluster evolution along route 1 and route 2. (a) AAoD. (b) AAoA.

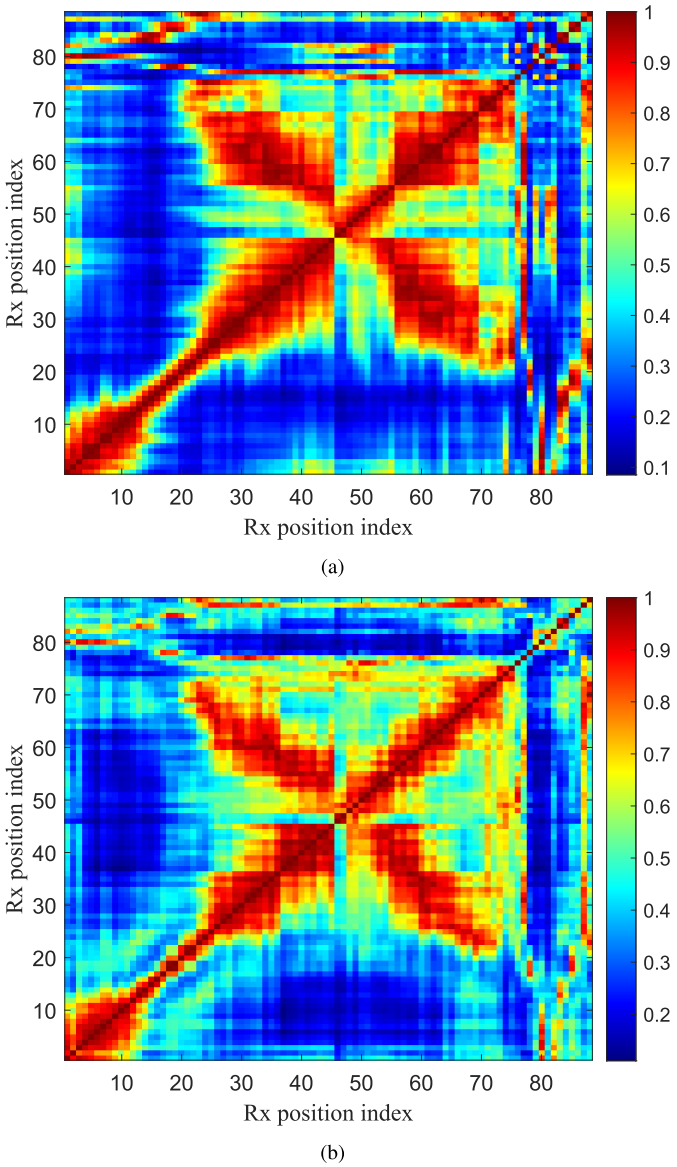

Fig. 12. Multilink correlation of APSD. (a) AoD. (b) AoA.

positions are LOS positions. The delay indices of LOS path are all shifted to 30. It can be seen that there is a slight variation in LOS power, and the reflection paths exhibit cluster birth–death process. The obvious delay trajectories of MPCs are owing to the relative movement between the Rx and the scatterers.

Fig. 11 demonstrates the drifting processes of the AAoA and AAoD along the two routes. The AAoA and AAoD are estimated and calculated in their own LCSs, respectively. RxH45 is the end of route 1 and RxH46 is the start of route 2. Hence, there is a break point between them. The power and delay of each path are denoted by the size and color of circles, respectively. The LOS path directions of measurement positions are calculated by Tx and Rx positions and shown by the color of manganese violet and the marker in "*." The estimated LOS angles match well with the calculated angles. In two routes, the Rx is approaching Tx first and then going away from Tx. As a result, the AAoA of the LOS path has the tendency to increase first and then decrease, and the AAoD of the LOS path decreases first and then increases. For LOS positions, the LOS path has the maximum power. For NLOS positions, the LOS path is obstructed and its power is lower than those of some reflection paths. These NLOS positions are distinguished in Fig. 11. It can be found that they have paths with similar directions, because they are close to each other and the maximum distance among them is 2.5 m. Compared with LOS positions, NLOS positions have more reflection paths with longer transmission distances.

Besides, we can note that the value of delay indices roughly can be classified into seven levels, i.e., D1: 31–34, D2: 35–38, D3: 39–41, D4: 42–46, D5: 46–50, D6: 50–60, and D7: 60–77. The level D1 is around the delay index of LOS path and the angles are scattered, so the clusters are mainly the metal surface near the Tx or Rx. The paths in levels D2 and D3 come from the pillars "P2-1" and "P3-1" as well as

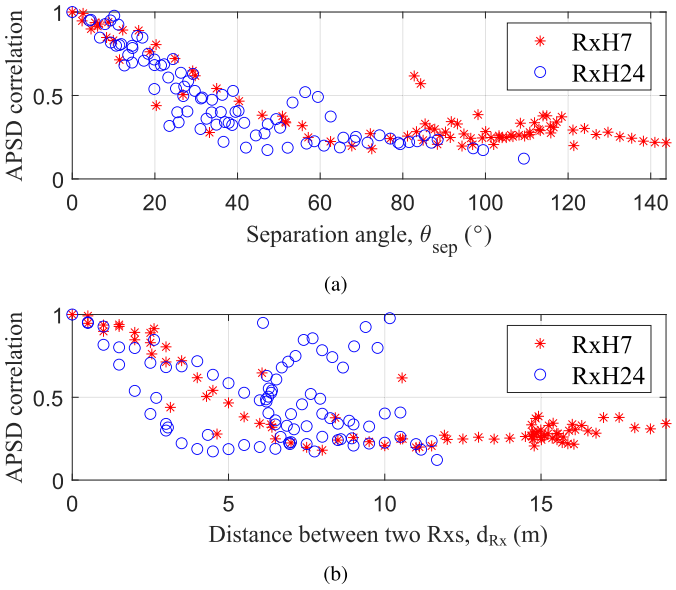

Fig. 13. Multilink APSD correlation of departure angle with θ_{sep} and d_{Rx} at RxH7 and RxH24. (a) Separation angle. (b) Distance between two Rxs.

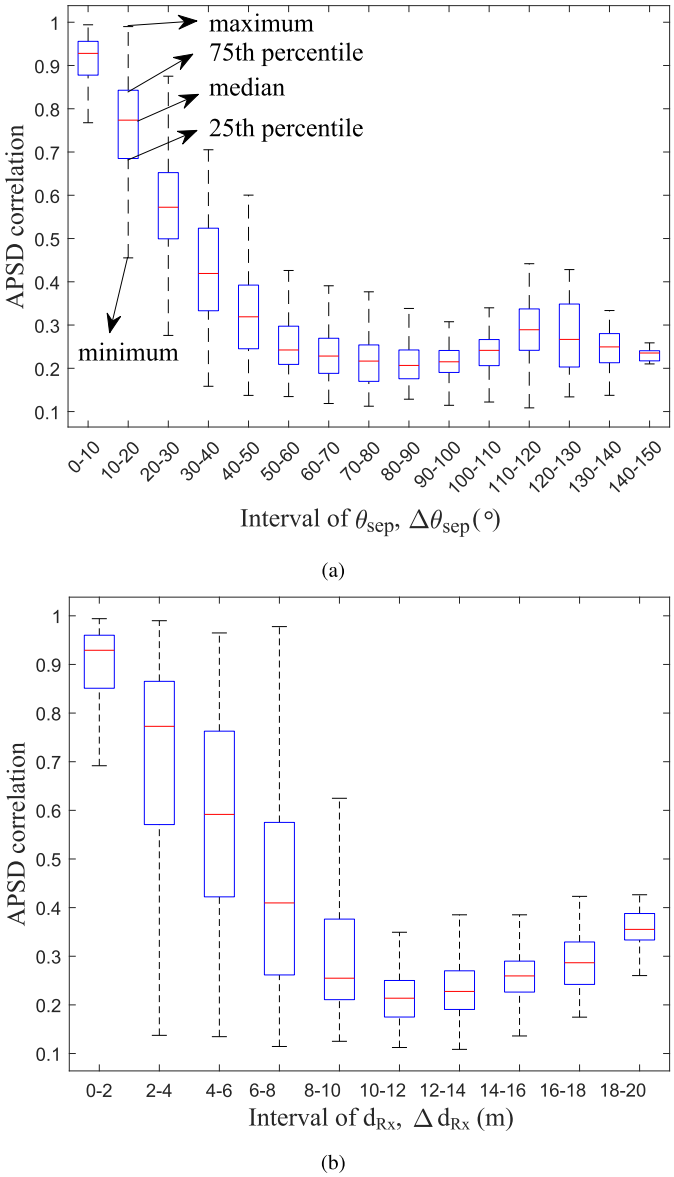

Fig. 14. Box plot of the multilink APSD correlation of departure angle with $\Delta\theta_{sep}$ and Δd_{Rx}. (a) Interval of separation angle. (b) Interval of distance.

the metal wall (wall 3) between them. Since the pillars and the Tx are static, the AAoD keeps near 36° and 120° for "P2-1" and "P3-1," respectively. The delay index changes along with Rx positions. The angles of Rx positions in levels D4 and D6 are close to each other, because they come from the pillar "P1-1" and the metal wall on the left side of the Tx (wall 1 in Fig. 4). Level D5 is due to the metal wall (wall 2) in the south of Rx. The AAoA and AAoD are around 270°. Level D7 has the largest delay index, and the corresponding paths are multireflection paths. We briefly mark the corresponding clusters in Fig. 11, and the MPCs show the obvious cluster birth–death process.

2) Multilink Correlation: Here, two indicators are given to measure how two links are correlated with each other, and the influencing factors of multilink correlations are presented. Bartlett spectrum [49] is one of the spectral-based methods used to perform angle estimation. Having known the array responses $\boldsymbol{c}(\boldsymbol{\Omega})$ of Tx and Rx antennas, the APSD can be given by

$$\mathbf{P}_{\mathrm{B}}(\boldsymbol{\Omega}) = \mathrm{tr}\left(\left|\hat{\boldsymbol{h}}(t)\boldsymbol{c}(\boldsymbol{\Omega})^{H}\left(\boldsymbol{c}(\boldsymbol{\Omega})\boldsymbol{c}(\boldsymbol{\Omega})^{H}\right)^{-1}\boldsymbol{c}(\boldsymbol{\Omega})\hat{\boldsymbol{h}}(t)^{H}\right|\right) \quad (12)$$

and

$$APSD = \mathbf{P}_{\mathrm{B}}(\boldsymbol{\Omega})/\|\mathbf{P}_{\mathrm{B}}(\boldsymbol{\Omega})\|_{\mathrm{F}} \quad (13)$$

where $\mathrm{tr}(\cdot)$ and $(\cdot)^{-1}$ mean the trace and inverse of a matrix, respectively. $\|\cdot\|_{\mathrm{F}}$ is the Frobenius norm. The correlation is calculated by vectorizing the APSD of any two links and then performing inner product computation. The multilink APSD correlation results of departure angle and arrival angle are shown in Fig. 12. The "1–88" at the x-axis or y-axis means the measurement positions index with the order marked in Fig. 4. The correlation coefficient is denoted by the color. The high correlation coefficients of diagonal positions in Fig. 12 indicate that there exists correlation between the APSD of different links. The correlated positions at the Tx side are more than that at the Rx side, because the propagation environment around Rx changes with Rx positions. Moreover, the high values of subdiagonal positions in Fig. 12 are mainly due to those spatially closed Rx positions. The correlation at the principle diagonal positions is high as well. We find that these positions are in close departure directions seen from the Tx, defined as the separation angle. This parameter is also investigated for LSPs' correlation in [28] and [29]. The results validate that if a Rx travels along a trajectory or if multiple Rxs are closely spaced, the angles and powers are correlated.

Fig. 13 is the APSD correlation of departure angle of RxH7 and RxH24 with other positions, which explains the effects of the distance between users d_{Rx} and separation angle θ_{sep}. The correlation of RxH7 decreases with the increase in separation angle and distance but the correlation of RxH24 only decreases

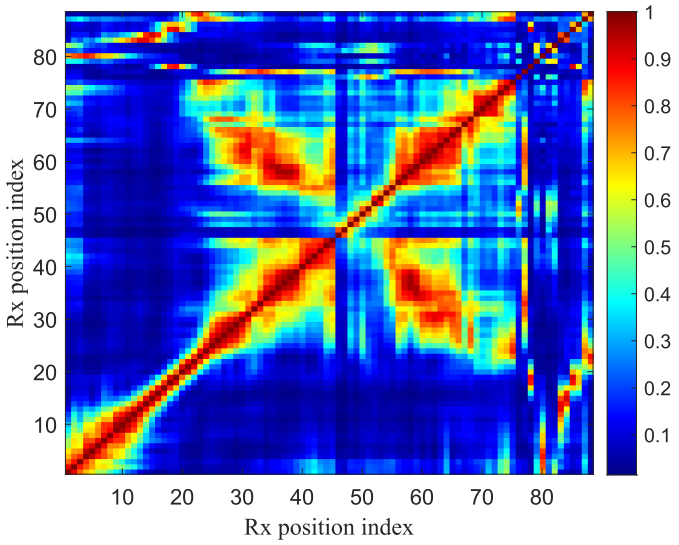

(a)

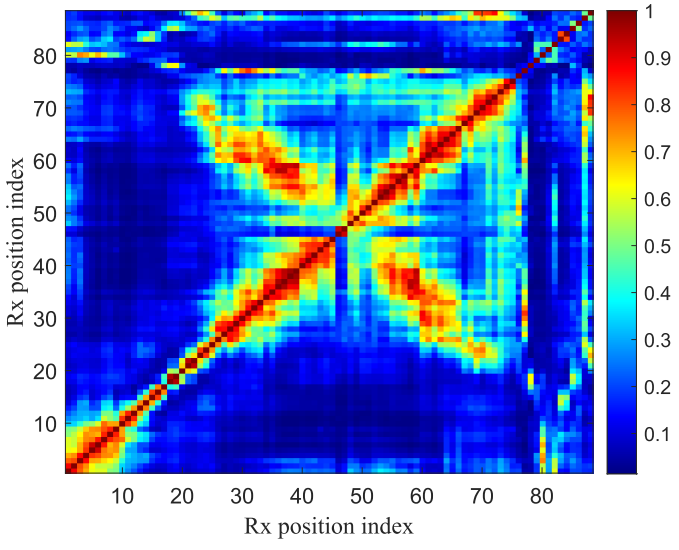

(b)

Fig. 15. Multilink CMC. (a) Tx side. (b) Rx side.

with the increasing separation angle. Because the Rx position sets {1–13, 80} are correlated with RxH7 with correlation coefficient above 0.7, and these positions have both smaller distance and smaller separation angle with RxH7. The Rx position sets {22–25, 27–28, 66–72, 87–88} are correlated with RxH24 with APSD correlation coefficient above 0.7. The positions' RxH66–72 and 87–88 have smaller separation angle but larger distance with RxH24. Hence, we attribute the high correlation at partial subdiagonal positions in Fig. 12 to the small separation angle. The positions RxH7 and RxH24 are LOS positions. However, their APSDs show similarity with those of some NLOS positions. The APSDs of other LOS positions also have correlations with those of some NLOS positions. For NLOS positions RxH70–75 and RxH87, multilink APSD correlation also exists when two Rxs have small separation angle and/or distance. For example, the Rx position sets {22–26, 28, 32–33, 63–73, 87–88} are correlated with RxH70, and their APSD correlation coefficients are above 0.7. In summary, the multilink APSD correlation is mainly influenced by the distance and separation angle between users and is independent of the LOS and NLOS status.

Fig. 14 is the box plot of multilink APSD correlation at the Tx side. It consists of five numerical points: minimum, 25th percentile, median, 75th percentile, and maximum. We can find that the median decreases with the increase in the separation angle and distance. The distance between the minimum and maximum, and the interquartile range of Fig. 14(b) are larger than those of Fig. 14(a). It turns out that the separation angle is a better factor to describe the multilink APSD correlation of departure angle. The multilink APSD correlation of arrival angle has the same conclusions.

The CMC of different links can be used to evaluate the multilink correlation effectively. The CMC is expressed as [35]

$$CMC = \frac{\left|\mathrm{tr}\{\mathbf{R}_1\mathbf{R}_2^H\}\right|}{\|\mathbf{R}_1\|_\mathrm{F}\|\mathbf{R}_2\|_\mathrm{F}} \tag{14}$$

where $\mathbf{R}_i$ is the correlation matrix of the ith link. The closer CMC is to 1, the higher the correlation between the two links is. Fig. 15 is the illustration of CMC results at the Tx side and Rx side. The CMC results show similar behaviors as the APSD correlation in Fig. 12, because the correlation matrix and APSD correlation are intrinsically correlated. The values of CMC are much lower than the correlation coefficient of APSD. The reason is that the CMC includes the influence of the antenna pattern, which may decrease the correlation.

V. Conclusion

In this article, we have presented extensive WLAN channel measurements and characteristics analysis in an indoor office environment. Channel parameters of PL, SF, DS, and KF have been analyzed for SISO channel measurements. The time nonstationarity and multilink correlation have been investigated for MIMO channel measurements.

The multifrequency SISO channel measurements have been conducted at three Wi-Fi bands under the same measurement conditions. The PL statistics at 5.5 and 6.5 GHz are similar, while the PL at 3 GHz is much smaller than those at 5.5 and 6.5 GHz. It has been shown that the SF and DS have no frequency dependence. The KF decreases with the increasing frequency in the LOS scenarios but exhibits no frequency dependence in the NLOS scenarios. In addition, the DS increases with the increasing distance between the Tx and the Rx in both the LOS and NLOS scenarios, and therefore can be modeled by a frequency-independent log-distance model. These results are helpful for the multifrequency cooperation technology in the next-generation Wi-Fi 7 communication systems.

SISO channel measurements with different HPBWs of antennas have been performed at 5.5 GHz in the AP–UE and AP–AP scenarios. For omnidirectional antennas, the PLE increases with the increase in the EHPBW, and the SF is independent of the EHPBW in the AP–UE scenario. Besides, the PL increases with the narrower EHPBW of omnidirectional

antennas. Directional antennas have smaller PL and larger SF because of their high gains and directionality. The comparisons of different antenna HPBWs are instructive for AP antenna selection and deployment in HD scenarios.

Multilink correlation from a new perspective of APSD has been investigated based on MIMO channel measurements at 5.5 GHz. Compared with the multilink correlation of APSD, the CMC may underestimate the correlation because of the effect of antenna patterns. The results have shown that the multilink correlation decreases with the increasing distance between users and separation angle. Moreover, the DPSD and angle drifting results have validated the time nonstationarity. Therefore, the smooth time evolution and the multilink correlations of SSPs need to be considered to guarantee the accuracy of channel simulations.

REFERENCES

[1] H. Pirayesh, P. K. Sangdeh, and H. Zeng, "Coexistence of Wi-Fi and IoT communications in WLANs," *IEEE Internet Things J.*, vol. 7, no. 8, pp. 7495–7505, Aug. 2020.

[2] C.-X. Wang et al., "On the road to 6G: Visions, requirements, key technologies and testbeds," *IEEE Commun. Surveys Tuts.*, early access, Feb. 27, 2023, doi: 10.1109/COMST.2023.3249835.

[3] F. Guo, F. R. Yu, H. Zhang, X. Li, H. Ji, and V. C. M. Leung, "Enabling massive IoT toward 6G: A comprehensive survey," *IEEE Internet Things J.*, vol. 8, no. 15, pp. 11891–11915, Aug. 2021.

[4] C. X. Wang, J. Huang, H. Wang, X. Gao, X. You, and Y. Hao, "6G wireless channel measurements and models: Trends and challenges," *IEEE Veh. Technol. Mag.*, vol. 15, no. 4, pp. 22–32, Dec. 2020.

[5] E. Khorov, I. Levitsky, and I. F. Akyildiz, "Current status and directions of IEEE 802.11be, the future Wi-Fi 7," *IEEE Access*, vol. 8, pp. 88664–88688, 2020.

[6] C. Deng et al., "IEEE 802.11be Wi-Fi 7: New challenges and opportunities," *IEEE Commun. Surveys Tuts.*, vol. 22, no. 4, pp. 2136–2166, 4th Quart., 2020.

[7] D. Lopez-Perez, A. Garcia-Rodriguez, L. Galati-Giordano, M. Kasslin, and K. Doppler, "IEEE 802.11be extremely high throughput: The next generation of Wi-Fi technology beyond 802.11ax," *IEEE Commun. Mag.*, vol. 57, no. 9, pp. 113–119, Sep. 2019.

[8] M. Yang, B. Li, Z. Yan, and Y. Yan, "AP coordination and full-duplex enabled multi-band operation for the next generation WLAN: IEEE 802.11be (EHT)," in *Proc. 11th Int. Conf. Wireless Commun. Signal Process. (WCSP)*, Oct. 2019, pp. 1–7.

[9] R. Zhang, Q. Guo, J. Wang, Z. Zhong, and C. Li, "WLAN channel measurement in two classrooms for LOS and NLOS coverage," in *Proc. ICNC*, Honolulu, HI, USA, Feb. 2019, pp. 708–713.

[10] S. Brahmi, M. Yazid, and M. Omar, "Multiuser access via OFDMA technology in high density IEEE 802.11ax WLANs: A survey," in *Proc. 2nd Int. Conf. Embedded Distrib. Syst. (EDiS)*, Nov. 2020, pp. 105–110.

[11] D. Dupleich, R. Müller, S. Skoblikov, J. Luo, G. D. Galdo, and R. S. Thoma, "Multi-band double-directional 5G street canyon measurements in Germany," in *Proc. Eur. Conf. Netw. Commun. (EuCNC)*, Jun. 2019, pp. 123–127.

[12] D. Dupleich, R. Müller, and S. Skoblikov, "Multi-band indoor propagation characterization by measurements from 6 to 60 GHz," in *Proc. EuCAP*, Krakow, Poland, Apr. 2019, pp. 1–5.

[13] D. Dupleich et al., "Multi-band vehicle to vehicle channel measurements from 6 GHz to 60 GHz at 'T' intersection," in *Proc. IEEE 2nd Connected Automated Vehicles Symp. (CAVS)*, Sep. 2019, pp. 1–5.

[14] Y. L. C. De Jong, J. A. Pugh, M. Bennai, and P. Bouchard, "2.4 to 61 GHz multiband double-directional propagation measurements in indoor office environments," *IEEE Trans. Antennas Propag.*, vol. 66, no. 9, pp. 4806–4820, Sep. 2018.

[15] G. Zhang et al., "Modeling multi-frequency characteristics for classroom and Hall scenarios at 2–4, 9–11 and 27–29 GHz bands," *IEEE Access*, vol. 9, pp. 14549–14563, 2021.

[16] J. Choi, N. G. Kang, Y. S. Sung, J. S. Kang, and S. C. Kim, "Frequency-dependent UWB channel characteristics in office environments," *IEEE Trans. Veh. Technol.*, vol. 58, no. 7, pp. 3102–3111, Sep. 2009.

[17] C. Garcia-Pardo, J.-M. Molina-Garcia-Pardo, A. Garrido-Cervantes, J. D. Muhehe, and L. Juan-Llacer, "Frequency dependence of 2–5 GHz polarized UWB channel parameters in office environment," *IEEE Trans. Antennas Propag.*, vol. 60, no. 6, pp. 2970–2979, Jun. 2012.

[18] W. Q. Malik, D. J. Edwards, and C. J. Stevens, "Frequency dependence of fading statistics for ultrawideband systems," *IEEE Trans. Wireless Commun.*, vol. 6, no. 3, pp. 800–804, Mar. 2007.

[19] Z. Zhou, L. Zhang, X. Chen, C.-X. Wang, and J. Huang, "Multi-frequency wireless channel measurements and characteristics analysis in indoor corridor scenarios," in *Proc. IEEE 94th Veh. Technol. Conf. (VTC-Fall)*, Sep. 2021, pp. 1–5.

[20] J. Lee, K. Kim, J. Park, and M. Kim, "Analysis of the effect of antenna beamwidth on received power in large indoor environments based on millimeter-wave channel measurements," in *Proc. ISAP*, Oct. 2018, pp. 1–2.

[21] M.-D. Kim, J. Liang, J. Lee, J. Park, B. Park, and H. K. Chung, "Investigating the effect of antenna beamwidth on millimeter-wave channel charaterization," in *Proc. PURSI AP-RASC*, Aug. 2016, pp. 1–4.

[22] A. Hughes, "Measuring the impact of beamwidth on the correlation distance of 60 GHz indoor and outdoor channels," *IEEE Open J. Veh. Technol.*, vol. 2, pp. 180–193, 2021.

[23] M. K. Samimi and T. S. Rappaport, "Statistical channel model with multi-frequency and arbitrary antenna beamwidth for millimeter-wave outdoor communications," in *Proc. IEEE Globecom Workshops (GC Wkshps)*, Dec. 2015, pp. 1–7.

[24] J. Lee, K.-W. Kim, M.-D. Kim, J.-J. Park, and H. K. Chung, "Empirical investigation of antenna beamwidth effects on the ITU-R building entry loss (BEL) model based on 32 GHz measurements," in *Proc. 11th Global Symp. Millim. Waves (GSMM)*, May 2018, pp. 1–3.

[25] C.-X. Wang, Z. Lv, X. Gao, X. You, Y. Hao, and H. Haas, "Pervasive wireless channel modeling theory and applications to 6G GBSMs for all frequency bands and all scenarios," *IEEE Trans. Veh. Technol.*, vol. 71, no. 9, pp. 9159–9173, Sep. 2022.

[26] J. Bian, C.-X. Wang, Y. Liu, J. Tian, J. Qiao, and X. Zheng, "3D non-stationary wideband UAV-to-ground MIMO channel models based on aeronautic random mobility model," *IEEE Trans. Veh. Technol.*, vol. 70, no. 11, pp. 11154–11168, Nov. 2021.

[27] Y. Liu, C.-X. Wang, H. Chang, Y. He, and J. Bian, "A novel non-stationary 6G UAV channel model for maritime communications," *IEEE J. Sel. Areas Commun.*, vol. 39, no. 10, pp. 2992–3005, Oct. 2021.

[28] N. Jalden, P. Zetterberg, B. Ottersten, A. Hong, and R. Thoma, "Correlation properties of large scale fading based on indoor measurements," in *Proc. IEEE Wireless Commun. Netw. Conf.*, Mar. 2007, pp. 1894–1899.

[29] M. Kim, J. J. Park, H. K. Chung, and X. Yin, "Cross-correlation characteristics of multi-link channel based on channel measurements at 3.7 GHz," in *Proc. ICACT*, PyeongChang, South Korea, Feb. 2012, pp. 351–355.

[30] J. Poutanen, K. Haneda, V.-M. Kolmonen, J. Salmi, and P. Vainikainen, "Analysis of correlated shadow fading in dual-link indoor radio wave propagation," *IEEE Antennas Wireless Propag. Lett.*, vol. 8, pp. 1190–1193, 2009.

[31] M. Zhu, F. Tufvesson, and J. Medbo, "Correlation properties of large-scale parameters from 2.66 GHz multi-site macro cell measurements," in *Proc. IEEE VTC-Spring*, Budapest, Hungary, May 2011, pp. 1–5.

[32] T. Zhou, C. Tao, L. Liu, and K. Liu, "Investigation of cross-correlation characteristics for multi-link channels in high-speed railway scenarios," *China Commun.*, vol. 15, no. 8, pp. 108–117, Aug. 2018.

[33] T. Zhou, C. Tao, S. Salous, and L. Liu, "Joint channel characteristics in high-speed railway multi-link propagation scenarios: Measurement, analysis, and modeling," *IEEE Trans. Intell. Transp. Syst.*, vol. 20, no. 6, pp. 2367–2377, Jun. 2019.

[34] C. Oestges and N. Czink, "Empirical investigation of multi-link separation for indoor MIMO channels," in *Proc. IEEE 22nd Int. Symp. Pers., Indoor Mobile Radio Commun.*, Sep. 2011, pp. 945–949.

[35] T. Zhou, C. Tao, and L. Liu, "LTE-assisted multi-link MIMO channel characterization for high-speed train communication systems," *IEEE Trans. Veh. Technol.*, vol. 68, no. 3, pp. 2044–2051, Mar. 2019.

[36] L. Zhang, X. Chen, Z. Zhou, C.-X. Wang, C. Pan, and Y. Wang, "A novel 3D non-stationary multi-frequency multi-link wideband MIMO channel model," in *Proc. Int. Conf. Wireless Commun. Signal Process. (WCSP)*, Oct. 2020, pp. 1016–1021.

[37] *Study on 3D Channel Model for LTE*, Standard 3GPP TR 36.873, V12.7.0, Dec. 2017.

[38] J. Huang, C.-X. Wang, Y. Yang, Y. Liu, J. Sun, and W. Zhang, "Channel measurements and modeling for 400–600-MHz bands in urban and suburban scenarios," *IEEE Internet Things J.*, vol. 8, no. 7, pp. 5531–5543, Apr. 2021.

[39] V. Kristem et al., "3D MIMO outdoor-to-indoor propagation channel measurement," *IEEE Trans. Wireless Commun.*, vol. 16, no. 7, pp. 4600–4613, Jul. 2017.

[40] J. Huang, C.-X. Wang, H. Chang, J. Sun, and X. Q. Gao, "Multi-frequency multi-scenario millimeter wave MIMO channel measurements and modeling for B5G wireless communication systems," *IEEE J. Sel. Areas Commun.*, vol. 38, no. 9, pp. 2010–2025, Sep. 2020.

[41] A. F. Molisch and M. Steinbauer, "Condensed parameters for characterizing wideband mobile radio channels," *Int. J. Wireless Inf. Netw.*, vol. 6, no. 3, pp. 133–154, Jul. 1999.

[42] X. Yin, B. H. Fleury, P. Jourdan, and A. Stucki, "Polarization estimation of individual propagation paths using the sage algorithm," in *Proc. 14th IEEE Proc. Pers., Indoor Mobile Radio Commun. (PIMRC)*, Sep. 2003, pp. 1795–1799.

[43] G. R. MacCartney, S. Deng, and T. S. Rappaport, "Indoor office plan environment and layout-based mmWave path loss models for 28 GHz and 73 GHz," in *Proc. IEEE 83rd Veh. Technol. Conf. (VTC Spring)*, May 2016, pp. 1–6.

[44] K. Haneda, N. Omaki, T. Imai, L. Raschkowski, M. Peter, and A. Roivainen, "Frequency-agile pathloss models for urban street canyons," *IEEE Trans. Antennas Propag.*, vol. 64, no. 5, pp. 1941–1951, May 2016.

[45] *Study on Channel Model for Frequencies From 0.5 to 100 GHz*, Standard 3GPP TR 38.901, V16.1.1, Jan. 2020.

[46] R. Aminzadeh, A. Thielens, M. Zhadobov, L. Martens, and W. Joseph, "WBAN channel modeling for 900 MHz and 60 GHz communications," *IEEE Trans. Antennas Propag.*, vol. 69, no. 7, pp. 4083–4092, Jul. 2021.

[47] X. Zhou et al., "Indoor wideband channel measurements and analysis at 11 and 14 GHz," *IET Microw., Antennas Propag.*, vol. 11, no. 10, pp. 1393–1400, Aug. 2017.

[48] P. Tang, J. Zhang, A. F. Molisch, P. J. Smith, M. Shafi, and L. Tian, "Estimation of the K-factor for temporal fading from single-snapshot wideband measurements," *IEEE Trans. Veh. Technol.*, vol. 68, no. 1, pp. 49–63, Jan. 2019.

[49] M. Aktar, B. Sankur, and Y. Istefanopulos, "Maximum likelihood and Bartlett spectrum estimates," in *Proc. IEEE Int. Conf. Acoust., Speech, Signal Process.*, Mar. 1984, pp. 566–568.

Li Zhang (Student Member, IEEE) received the B.E. degree from Hunan University, Changsha, China, in 2019. She is currently pursuing the Ph.D. degree with the National Mobile Communications Research Laboratory, Southeast University, Nanjing, China.

Her research interests include indoor channel measurements, characteristics analysis, and modeling.

Cheng-Xiang Wang (Fellow, IEEE) received the B.Sc. and M.Eng. degrees in communication and information systems from Shandong University, Jinan, China, in 1997 and 2000, respectively, and the Ph.D. degree in wireless communications from Aalborg University, Aalborg, Denmark, in 2004.

He was a Research Assistant with the Hamburg University of Technology, Hamburg, Germany, from 2000 to 2001; a Visiting Researcher with Siemens AG Mobile Phones, Munich, Germany, in 2004; and a Research Fellow with the University of Agder, Grimstad, Norway, from 2001 to 2005. He has been with Heriot-Watt University, Edinburgh, U.K., since 2005, where he was promoted to a Professor in 2011. In 2018, he joined Southeast University, Nanjing, China, as a Professor. He is also a part-time Professor with the Purple Mountain Laboratories, Nanjing. He has authored four books, three book chapters, and more than 500 papers in refereed journals and conference proceedings, including 27 highly cited papers. He has also delivered 24 invited keynote speeches/talks and 15 tutorials in international conferences. His current research interests include wireless channel measurements and modeling, 6G wireless communication networks, and electromagnetic information theory.

Dr. Wang is a member of the Academia Europaea (The Academy of Europe) and the European Academy of Sciences and Arts (EASA); a fellow of the Royal Society of Edinburgh (FRSE), IET, and the China Institute of Communications (CIC); an IEEE Communications Society Distinguished Lecturer in 2019 and 2020; a Highly Cited Researcher recognized by Clarivate Analytics from 2017 to 2020. He has received 15 Best Paper Awards from IEEE Global Communications Conference (GLOBECOM) 2010, IEEE International Conference on Communication Technology (ICCT) 2011, International Conference on Intelligent Transport System Telecommunications (ITST) 2012, IEEE Vehicular Technology Conference (VTC)-Spring 2013, International Wireless Communications and Mobile Computing Conference (IWCMC) 2015, IWCMC 2016, IEEE/CIC International Conference on Communications in China (ICCC) 2016, International Symposium on Wireless Personal Multimedia Communications (WPMC) 2016, Wireless and Optical Communications Conference (WOCC) 2019, IWCMC 2020, International Conference on Wireless Communications and Signal Processing (WCSP) 2020, International Conference on Communications, Signal Processing, and Systems (CSPS) 2021, WCSP 2021, and IEEE/CIC ICCC 2022. He has served as a TPC member, the TPC Chair, and the General Chair for more than 80 international conferences. He has served as an Editor for more than ten international journals, including the IEEE TRANSACTIONS ON WIRELESS COMMUNICATIONS from 2007 to 2009, the IEEE TRANSACTIONS ON VEHICULAR TECHNOLOGY from 2011 to 2017, and the IEEE TRANSACTIONS ON COMMUNICATIONS from 2015 to 2017. He was a Guest Editor of the IEEE JOURNAL ON SELECTED AREAS IN COMMUNICATIONS, Special Issue on Vehicular Communications and Networks (Lead Guest Editor), Special Issue on Spectrum and Energy Efficient Design of Wireless Communication Networks, and Special Issue on Airborne Communication Networks. He was also a Guest Editor for the Special Issue on Wireless Big Data of the IEEE TRANSACTIONS ON BIG DATA. He is an Executive Editorial Committee Member of the IEEE TRANSACTIONS ON WIRELESS COMMUNICATIONS. He is also a Guest Editor for the Special Issue on Intelligent Resource Management for 5G and Beyond For the IEEE TRANSACTIONS ON COGNITIVE COMMUNICATIONS AND NETWORKING.

Zihao Zhou received the B.E. degree from the Nanjing University of Posts and Telecommunications, Nanjing, China, in 2019. He is currently pursuing the Ph.D. degree with the National Mobile Communications Research Laboratory, Southeast University, Nanjing.

His research interests include channel parameters' estimation and multifrequency channel measurements, characteristics analysis, and modeling.

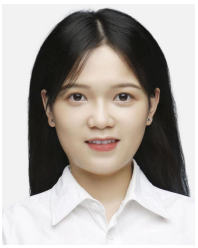

Xinyue Chen (Student Member, IEEE) received the B.E. degree in communication engineering from the University of Electronic Science and Technology of China, Chengdu, China, in 2019, and the M.Sc. degree in information and communication engineering from Southeast University, Nanjing, China, in 2022.

Her research interests include massive multiple-input–multiple-output (MIMO) channel characterization, measurement, and modeling.

Jie Huang (Member, IEEE) received the B.E. degree in information engineering from Xidian University, Xi'an, China, in 2013, and the Ph.D. degree in information and communication engineering from Shandong University, Jinan, China, in 2018.

From October 2018 to October 2020, he was a Post-Doctoral Research Associate with the National Mobile Communications Research Laboratory, Southeast University, Nanjing, China, supported by the National Postdoctoral Program for Innovative Talents, where he has been an Associate Professor since November 2020. From January 2019 to February 2020, he was a Post-Doctoral Research Associate with Durham University, Durham, U.K. Since March 2019, he has been a part-time Researcher with the Purple Mountain Laboratories, Nanjing. He has authored and coauthored more than 70 papers in refereed journals and conference proceedings. His research interests include millimeter-wave, massive multiple-input–multiple-output (MIMO), reconfigurable intelligent surface channel measurements and modeling, wireless big data, and 6G wireless communications.

Dr. Huang has received the Best Paper Awards from International Symposium on Wireless Personal Multimedia Communications (WPMC) 2016, International Conference on Wireless Communications and Signal Processing (WCSP) 2020, and WCSP 2021. He has delivered eight tutorials in IEEE/China Institute of Communications (CIC) International Conference on Communications in China (ICCC) 2021, IEEE International Symposium on Personal Indoor and Mobile Radio Communications (PIMRC) 2021, IEEE International Conference on Communications (ICC) 2022, IEEE Vehicular Technology Conference (VTC)-Spring 2022, IEEE/CIC ICCC 2022, IEEE VTC-Fall 2022, IEEE PIMRC 2022, and IEEE Global Communications Conference (GLOBECOM) 2022.

Chun Pan received the B.S. degree from Harbin Engineering University, Harbin, China, in 2010, and the Ph.D. degree from the Beijing University of Posts and Telecommunications, Beijing, China, in 2015.

He joined Huawei Technologies Company Ltd., Nanjing, China, in 2015. His research interests include signal processing techniques, radio propagation, wireless sensing, ultrahigh reliability transmission, and machine learning.

El-Hadi M. Aggoune (Life Senior Member, IEEE) received the M.Sc. and Ph.D. degrees in electrical engineering from the University of Washington (UW), Seattle, WA, USA, in 1984 and 1988, respectively.

He has served at several universities in USA and abroad at many academic ranks, including the Endowed Chair Professor. He is currently serving as a Professor and the Director of the Sensor Networks and Cellular Systems (SNCS) Research Center, University of Tabuk, Tabuk, Saudi Arabia. His research interests include wireless communication, sensor networks, power systems, neurocomputing, and scientific visualization.

Dr. Aggoune is listed as an Inventor in several patents, one of them assigned to the Boeing Company, USA. He is a Professional Engineer registered in the state of Washington. He has coauthored papers in IEEE and other journals and conferences and served on editorial boards and technical committees for many of them. He was a recipient of the IEEE Professor of the Year Award, UW. He was the Director of a laboratory that received the Boeing Supplier Excellence Award.

Yang Miao (Member, IEEE) received the M.Sc. and Ph.D. degrees from the Radio Propagation Laboratory, Mobile Communications Research Group, Tokyo Institute of Technology, Tokyo, Japan, in 2012 and 2015, respectively.

From 2010 to 2015, she was a Research Assistant with the Takada Laboratory, Tokyo Institute of Technology. From 2015 to 2018, she was a Post-Doctoral Researcher with the Institute of Information and Communication Technologies, Electronics, and Applied Mathematics, Universite Catholique de Louvain, Louvain-la-Neuve, Belgium, and IMEC, Wireless, Acoustics, Environment, and the Expert Systems Laboratory, Ghent University, Ghent, Belgium. From 2017 to 2018, she was a part-time Senior Antenna Engineer with Jaguar Radio Wave Corporation, Shenzhen, China. From 2018 to 2019, she was a Research Assistant Professor with the Southern University of Science and Technology, Shenzhen, China. Since August 2019, she has been an Assistant Professor with the Radio Systems Group, University of Twente, Enschede, The Netherlands. Since November 2021, she has been affiliated in part-time at Katholieke Universiteit (KU) Leuven, Leuven, Belgium, as a Marie Curie Individual Fellow. Her current research interests include joint communication and sensing, incorporating mobility, and human factors.